Atmos. Chem. Phys. Discuss., https://doi.org/10.5194/acp-2018-330
Manuscript under review for journal Atmos. Chem. Phys.
Discussion started: 23 April 2018

Atmospheric Chemistry and Physics
Open Access
Discussions

Stratospheric aerosol radiative forcing simulated by the chemistry climate model EMAC using aerosol CCI satellite data

Christoph Brühl[1], Jennifer Schallock[1], Klaus Klingmüller[1], Charles Robert[2], Christine Bingen[2], Lieven Clarisse[3], Andreas Heckel[4], Peter North[4]

[1]Max Planck Institute for Chemistry, Mainz, Germany; [2]BIRA Brussels, Belgium; [3]ULB Brussels, Belgium; [4]Swansea University, UK

Correspondence to: Christoph Brühl (christoph.bruehl@mpic.de)

Abstract. This paper presents decadal simulations of stratospheric and tropospheric aerosol by the chemistry general circulation model EMAC constrained with satellite observations in the framework of the ESA-Aerosol-CCI project like GOMOS (Global Ozone Monitoring by Occultation of Stars) and (A)ATSR ((Advanced) Along Track Scanning Radiometer) on the ENVISAT (European Environmental Satellite), and IASI (Infrared Atmospheric Sounding Interferometer) on Metop (Meteorological Operational Satellite).

The EMAC simulations with modal interactive aerosol and observations by GOMOS show that sulfate particles from about 230 volcanic eruptions identified mostly from MIPAS (Michelson Interferometer for Passive Atmospheric Sounding) SO_2 limb measurements dominate the interannual variability of aerosol extinction in the lower stratosphere, and of radiative forcing at the tropopause. To explain the observations, desert dust and organic and black carbon, transported to the lowermost stratosphere by the Asian summer monsoon and tropical convection, are also important. This holds also for radiative heating by aerosol in the lowermost stratosphere. Comparison with (A)ATSR total aerosol optical depth at different wavelengths and IASI dust optical depth shows that the model is able to represent stratospheric and tropospheric aerosol in a consistent way.

1. Introduction

Climate effects of stratospheric aerosols can be important, as analyzed for example by Solomon et al. (2011). Stratospheric aerosol exerts a negative radiative forcing on the troposphere because it reduces solar radiation reaching the surface and the lower atmosphere. In addition, changes in diffuse light fraction have shown their potential to enhance photosynthesis (Gu et al., 2003). The present study contributes to the SPARC/SSIRC initiative (Stratosphere-troposphere Processes And their Role in Climate/ Stratospheric Sulfur and Its Role in Climate). The multiple instrument satellite dataset provided in the Climate Change Initiative (CCI) of the European Space Agency (ESA) (Popp et al., 2016) is very valuable for evaluation and improvement of the treatment of stratospheric and tropospheric aerosols in global chemistry climate models, like for example the one used by Brühl et al. (2015), EMAC (ECHAM5/MESSy Atmospheric Chemistry). The datasets providing extinctions or total optical depth at wavelengths from ultraviolet (UV) to terrestrial infra-red (IR) are very useful to validate and optimize assumptions on the size distribution and on the composition of aerosol in the model, but also on aerosol sources. Some aspects of the stratospheric part of this study have been addressed in Bingen et al. (2017). The ATSR and IASI datasets provide additional constraints on tropospheric aerosol, especially desert dust, which can penetrate the tropopause via the Asian Summer Monsoon system.

In Section 2, we briefly present the satellite datasets used to feed the model: GOMOS, IASI and (A)ATSR. Further, in Section 3 we briefly describe the EMAC model and the various versions used in our work. In Section 4, we analyze the impact of the main aerosol sources on the upper tropospheric and lower stratospheric aerosol burden. The influence of volcanic sources derived from satellite data, but also of dust and organic aerosols is described. We present examples on the constraints by satellite observations in different spectral regions on different aerosol types with respect to particle size and composition. Finally, we discuss the evolution of the optical depth and radiative forcing by stratospheric aerosols. Conclusions are drawn in Section 5.

2. Satellite data products from Aerosol_cci II

2.1. GOMOS (Global Ozone Monitoring by Occultation of Stars)

GOMOS is an instrument based on the stellar occultation technique (Bertaux et al., 2010) and provides atmospheric measurements in the UV-Visible range. The use of stellar occultation results in a high rate of occultation measurements, and consequently, a very good spatial coverage compared to solar occultation. As a drawback, the signal-to-noise ratio of each measurement is much lower than in the solar case, and varies with the star characteristics (especially its magnitude and its temperature). The operational retrieval, IPF, provides density profiles for trace gases such as O_3 (ozone), NO_2 (nitrogen dioxide), and NO_3 (nitrogen trioxide) (Kyrola et al., 2010), as well as aerosol extinction. However, the extinction shows a poor quality out of the reference wavelength at 500 nm. For this reason an alternative inverse algorithm called AerGOM was developed specifically to optimize the aerosol retrieval (Vanhellemont et al., 2016; Robert et al., 2016). AerGOM provides as primary aerosol quantity the extinction coefficient and its spectral dependence, currently over the range 250-750 nm.

From the AerGOM extinction, climate data records (CDRs) were developed in the framework of the ESA Aerosol CCI project for different quantities including the aerosol extinction and the related aerosol optical depth at several wavelengths (355, 440, 470, 550 and 750 nm, Bingen et al., 2017). In their current version (version 3.0), these CDRs are defined on a grid with a resolution of 5° in latitude, 60° in longitude, 1 km in altitude, and 5-day time period. The records cover the whole ENVISAT period (March 2002 - April 2012) and include the total aerosol extinction, but also the polar stratospheric cloud (PSC) fraction and the non-cloud fraction which can be attributed, in good approximation, to sulfate aerosols below an altitude of 35 km. The grid resolution was chosen to ensure a reasonable statistical sampling in most of the grid cells, and to optimally reflect the typical transport of volcanic plumes after an eruption reaching the upper troposphere or the stratosphere, by providing a good coherence between longitudinal and latitudinal air mass transports, and a temporal resolution enabling the detection of volcanic signatures. The development work of these CDRs showed the importance of such a high temporal resolution to derive a realistic estimate of the impact of all volcanic eruptions on the stratospheric aerosol burden: when large temporal intervals are used (such as in the very common case of monthly means), the aerosol signature is diluted in the averaging process of the gridded extinction value or even gets lost, and the contribution of volcanic aerosols to the gridded extinction is underestimated. This effect has a significant impact when the CDRs are used to constrain climate models.

2.2. IASI (Infrared Atmospheric Sounding Interferometer)

The IASI dust dataset of the Université Libre de Bruxelles (ULB) was generated in the context of ESA CCI's project (Popp et al., 2016). It is based on a statistical regression technique and the use of a neural network trained on synthetic IASI data. A similar scheme has already been applied for the retrieval of NH_3 (ammonia) (Whitburn et al., 2016 and Van Damme et al., 2017). As input variables it uses the IASI L2 pressure, humidity and temperature information, spectral information and a CALIPSO (Cloud-Aerosol Lidar and Infrared Pathfinder Satellite Observation) derived dust altitude climatology. The main output variables are dust optical depth at 10 and 11 µm (and 550 nm). Initial results and validation performance are provided in (Popp et al., 2016).

2.3. (A)ATSR ((Advanced) Along Track Scanning Radiometer)

The ATSR (SU) algorithm has been developed at Swansea University for estimation of atmospheric aerosol and surface reflectance for the ATSR-2, AATSR sensors, and SLSTR (Sea and Land Surface Temperature Radiometer) on Sentinel-3. Over land, the algorithm employs a parameterized model of the surface angular anisotropy (North, 2002), and uses the dual-view capability of the instrument to allow aerosol property estimation without a priori assumptions on surface spectral reflectance. Over ocean, the algorithm uses a simple a priori model of ocean surface reflectance at both nadir and along-track view angles. A climatology (Kinne et al., 2006) is used to constrain chemical composition of the aerosol components at 1° x 1° latitude-longitude grid, while the method retrieves aerosol size and optical thickness on a 10 km grid. The algorithm has been developed from initial prototype (Bevan et al., 2012) under the Aerosol CCI program, and results and validation performance for version 4.21 are provided in Popp et al. (2016). The version used here (V4.3) differs from that summarized in Popp et al. (2016) by improvements in retrieval of coarse/fine mode fraction, and improved cloud screening over ocean in the region of dense plumes, resulting in approximately 10% greater coverage, with small improvement in correlation against AERONET (AErosol RObotic NETwork) values.

3. Model Setup

For the simulations of the radiative and chemical effects of stratospheric aerosol, the ECHAM5 (5th generation of European Centre Hamburg general circulation model) general circulation model coupled to the Modular Earth Submodel System Atmospheric Chemistry (EMAC) was used (Brühl et al., 2015, updated to the version of Jöckel et al., 2010). As dust reaching the upper troposphere/lower stratosphere region (UTLS) is sensitive to model resolution, we used different model resolutions to improve the dust simulations: the standard T42 resolution (spectral, 2.75° in latitude and longitude), T63 resolution (1.88°) and T106 resolution (1.1°). The vertical grid has 90 layers from the surface up to 0.01 hPa (~80 km altitude) with finest resolution in the boundary layer and near the tropopause. For T106 only test simulations with the low top model version with 31 levels up to 30 km altitude are discussed here. The simulations were performed for the ENVISAT time period from July 2002 to March 2012 to allow for the use of data from MIPAS, GOMOS, and ATSR for input and validation. The period from 1997 to 2002 using SAGE II (Stratospheric Aerosol and Gas Experiment) was simulated first to get consistent initial conditions.

The applied aerosol module GMXE (Pringle et al., 2010) accounts for seven modes using lognormal size distributions (nucleation mode, soluble and insoluble Aitken, accumulation and coarse modes). The boundary between accumulation mode and coarse mode, a model parameter, is set at a particle radius of 1.6 µm to avoid too fast sedimentation in case of major volcanic eruptions. For dust sensitivity studies in T106 also a boundary of 1.0 µm is used. Optical properties for the types sulfate, dust, organic and black carbon (OC and BC), sea salt, and aerosol water are calculated and used in radiative transfer calculations which (except for the T106 low top sensitivity studies) feedback to atmospheric dynamics. Desert dust simulations are based on the emission schemes by Astitha et al. (2012) and Klingmüller et al. (2018). Aerosol module parameters, like for example, the composition of sea salt, were optimized on the basis of the satellite data.

SO_2 plumes (sulfur dioxide) from about 230 explosive volcanic eruptions into the stratosphere were derived from 3-dimensional data fields of MIPAS and GOMOS on ENVISAT with a temporal resolution of 5 days, and superimposed to the simulated SO_2 at the time of the eruption. Each identified volcanic eruption (with names from the Smithsonian volcanic database, www.volcano.si.edu) is listed in an emission inventory published recently (Bingen et al., 2017), which provides an estimate of the altitude and the amount of SO_2 injected into the atmosphere. Boundary conditions for background concentrations of SO_2 from outgassing volcanoes into the troposphere are taken from the climatology of Diehl et al. (2012) truncated at 200 hPa to avoid double counting. The sulfur source gas OCS (carbonyl sulfide) is constrained by observed zonal average surface volume mixing ratios (update of the data by Montzka et al., 2007). Marine DMS (dimethyl sulfide) as natural sulfur source is also included in the model. For anthropogenic emissions of CO (carbon monoxide), NOx (nitrogen oxides), sulfur, OC, and BC the DLR-MACCity emission inventory is used. Biomass burning is based on ACCMIP-MACCity and GFEDv2, OC-SOA (secondary organic aerosol) on AEROCOM_UMZ1. For details on the emission inventories see Jöckel et al. (2016).

4. Stratospheric Aerosol and its radiative effect

4.1. Volcanic eruptions

Volcanic emissions have a large impact on the stratospheric aerosol burden. Even small and moderate eruptions contribute to the stratospheric aerosol load due to transport and accumulation of sulfate aerosol. Volcanic SO_2 injections explain most of the interannual variability of stratospheric aerosol extinction (decadal logarithm) observed by GOMOS at 3 wavelengths, as depicted in Fig. 1 for the altitude dependence in the tropics. Comparisons for the latitude dependence in the lower stratosphere are shown in Bingen et al. (2017) for 550 nm (b), the wavelength, where the GOMOS data quality is best. The eruptions of Nabro in June 2011 and the successive eruptions of Soufriere Hills and Rabaul in 2006 have the largest effects on extinction in the lower stratosphere.

4.2. Dust and organics from the troposphere in the upper troposphere/lower stratosphere (UTLS)

Extinction in the lowermost stratosphere and upper troposphere is mostly due to desert dust and organic carbon aerosol. These contributions were strongly underestimated in Brühl et al. (2015) due to a crude parameterization in the used model version based on Jöckel et al. (2006). To reproduce the GOMOS observations of extinction at the 3 different wavelengths it is essential to account for dust in a proper way, also with respect to particle size. Dust reaching the UTLS is sensitive to model resolution, mostly via the convection parameterization. In Fig. 1 the simulated extinction with the dust contribution in T42 downscaled to the values in T63 resolution (i.e. with a scaling factor of 1/3) fits best to the GOMOS observations. Fig. 2 shows observed and simulated extinction in the Asian sector at 17 km. The largest extinction values are found at the location and time of the Asian summer monsoon. This feature is clearest in years not perturbed by medium strength volcanic eruptions, like for example 2010. The corresponding zonal average extinction is illustrated in Bingen et al. (2017). Results with the full, not downscaled dust (overestimate) and without dust at all and without organic carbon (underestimate) are shown in the supplement.

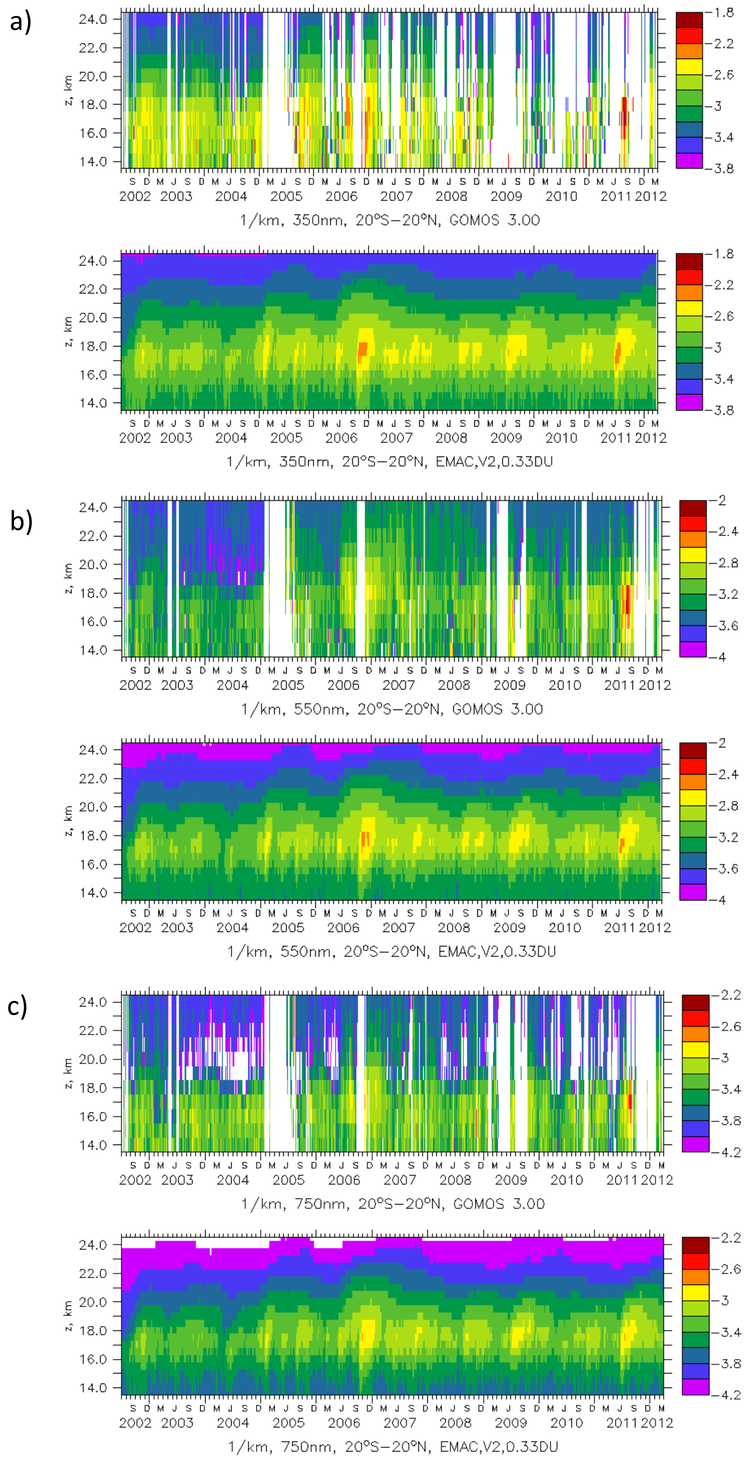

Figure 1: GOMOS and EMAC extinctions (log) in the tropics as function of altitude for different wavelengths: (a) UV 350 nm, (b) visible 550 nm and (c) near infrared 750 nm; dust in EMAC resolution T42 downscaled to results in resolution T63

Observations by IASI and ATSR indicate a maximum in dust aerosol optical depth (DAOD) in early northern hemispheric summer over the Asian deserts located in the inflow regions of the monsoon (see section 4.4). A similar feature is found in the simulations by EMAC. This supports our findings that desert dust is also important for the UTLS.

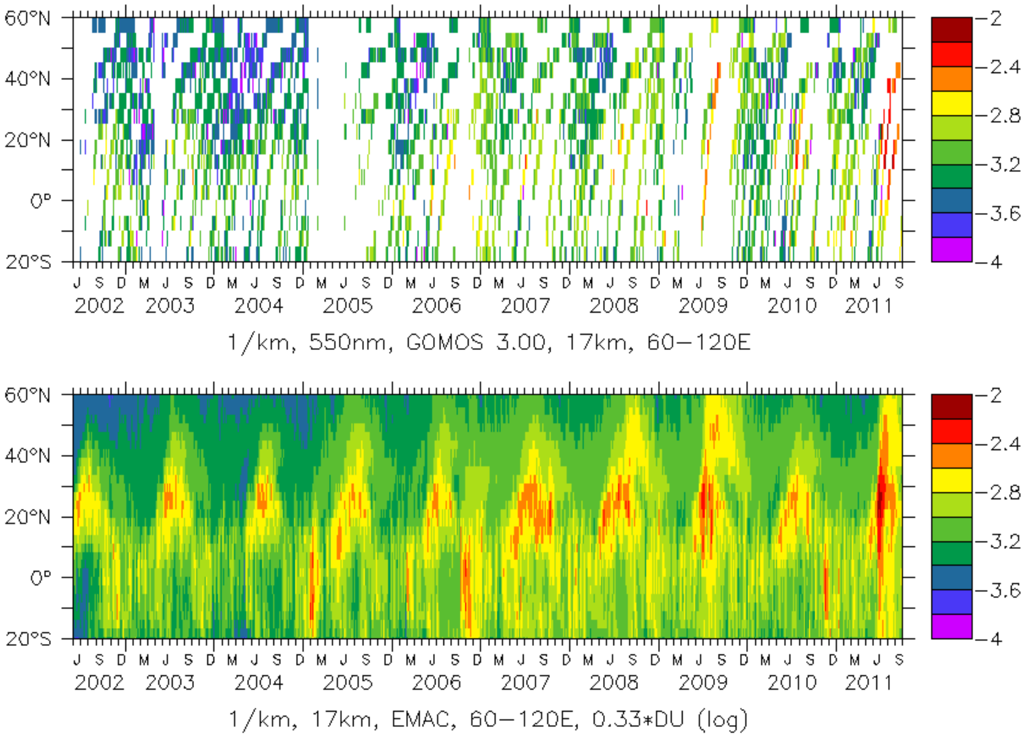

Figure 2: Observed (top) and simulated (bottom) extinction in the Asian sector (60°E-120°E, 20°S-60°N).

4.3. Stratospheric aerosol radiative forcing and total optical depth of stratospheric aerosol

Desert dust transported to the UTLS mostly via the Asian summer monsoon contributes significantly to the seasonal cycle of total stratospheric aerosol optical depth in satellite observations and the EMAC simulations shown in Fig. 3 for the tropics (middle panel) and for midlatitudes (bottom panel). Global radiative forcing at the tropopause is depicted in the upper panel. The figure contains in black results from the old model version with less volcanoes (Brühl et al., 2015) and in blue the old model version with about the same volcanic input as in Bingen et al. (2017). Green lines and symbols show estimates derived from satellite observations like SAGE II, OSIRIS (Optical Spectrograph and InfraRed Imaging System) and CALIPSO (Solomon et al., 2011; Santer et al., 2014; Bourassa et al., 2012). Red shows results of the current model version with the Astitha et al. (2012) dust scheme. Especially in Northern summer these aerosol optical depths (AOD) appear high because in standard horizontal resolution T42 the convective transport of dust to the UTLS in the Asian monsoon region is overestimated. This is clearly seen in Fig. 4 which shows in black the observations by GOMOS. Using the higher resolution T63, for which the convection parameterization was developed, the agreement to the satellite observations is much better (Fig. 4, purple), especially at midlatitudes.

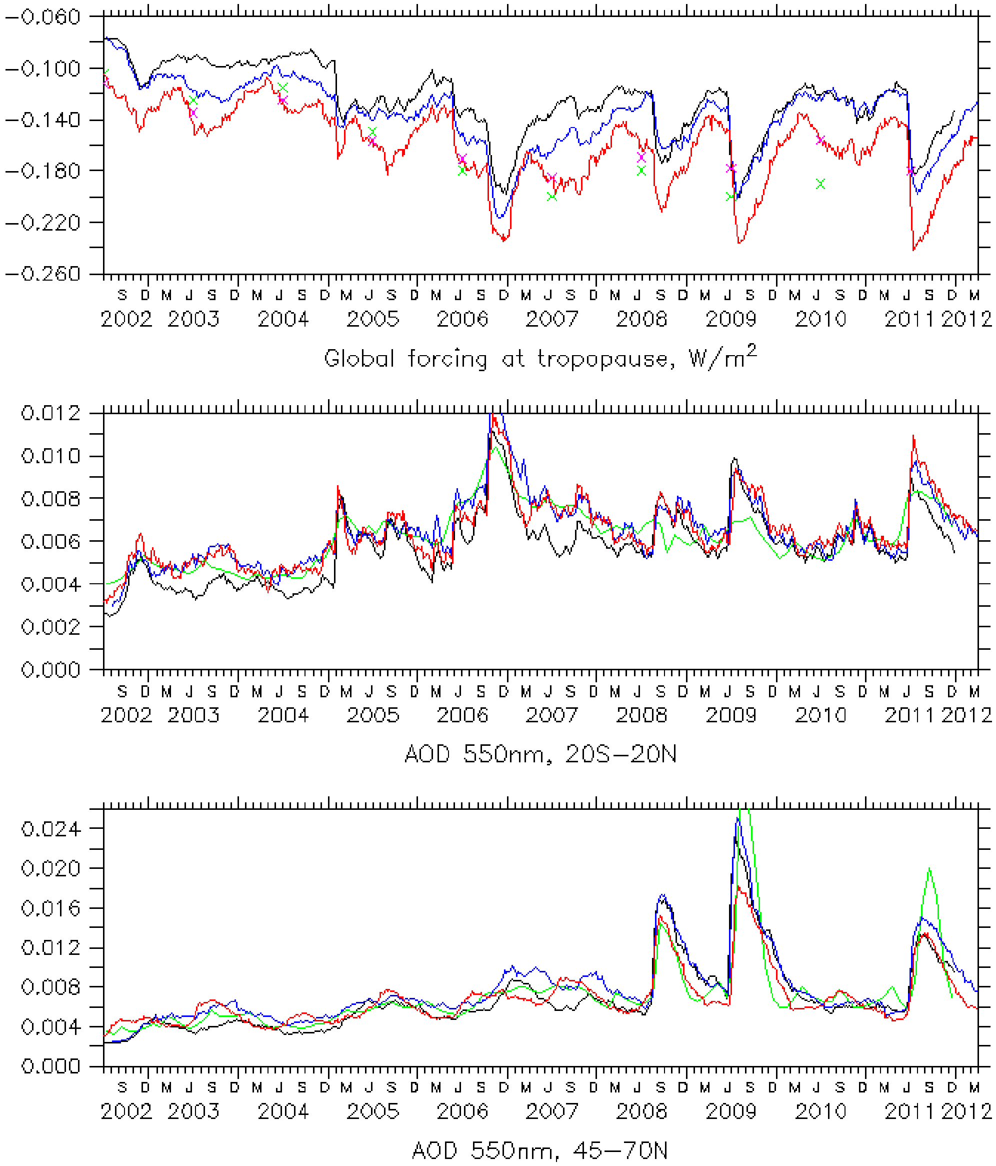

Global forcing at tropopause, W/m^2

AOD 550nm, 20S−20N

AOD 550nm, 45−70N

Figure 3: Stratospheric aerosol radiative forcing and stratospheric AOD. Red lines and purple crosses: EMAC, resolution T42, current version (Bingen et al., 2017); black: EMAC, version used in Brühl et al. (2015); blue: As black, but with more volcanoes; green: From observations (crosses annual mean for forcing (Solomon et al., 2011), SAGE II, CALIPSO, OSIRIS).

Atmos. Chem. Phys. Discuss., https://doi.org/10.5194/acp-2018-330
Manuscript under review for journal Atmos. Chem. Phys.
Discussion started: 23 April 2018

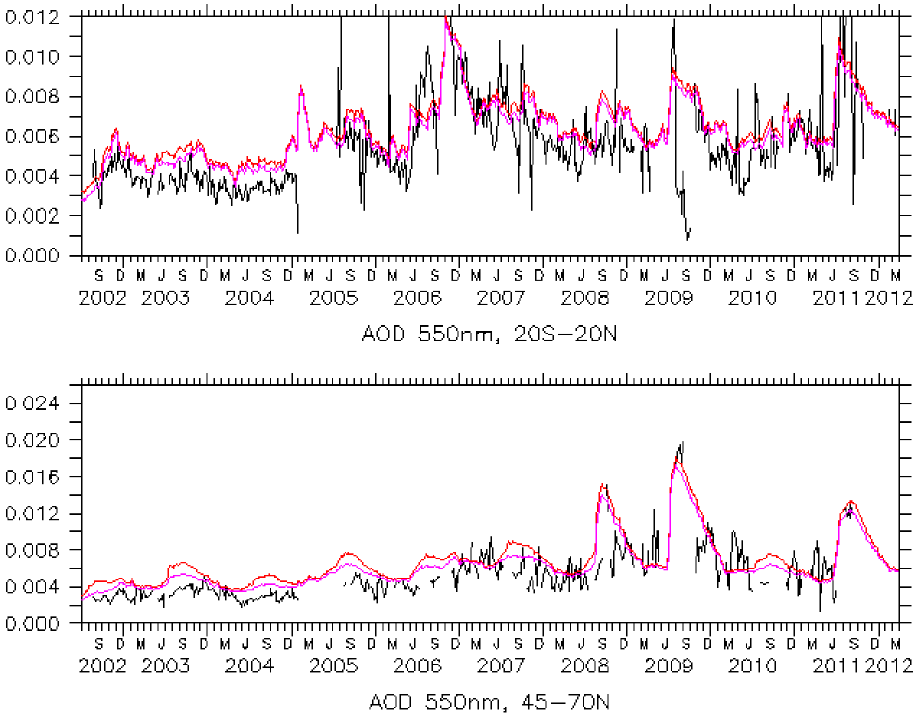

Figure 4: Stratospheric AOD observed by GOMOS (black) and simulated by EMAC in resolutions T42 (red) and T63 (purple). The simulations differ mostly by dust transported to the UTLS.

The simulated aerosol radiative heating shown in Fig. 5 reflects the medium volcanic eruptions with the largest effects near 18 km. There, desert dust causes additional heating at the time of the Asian summer monsoon. In the UTLS below every year in September a clear signal from biomass burning organic aerosol is visible. Above, around 22 km, the dust below in northern hemispheric summer causes a reduction of absorption of terrestrial radiation by ozone. This effect is smaller in the simulation with higher horizontal resolution (T63) but still visible.

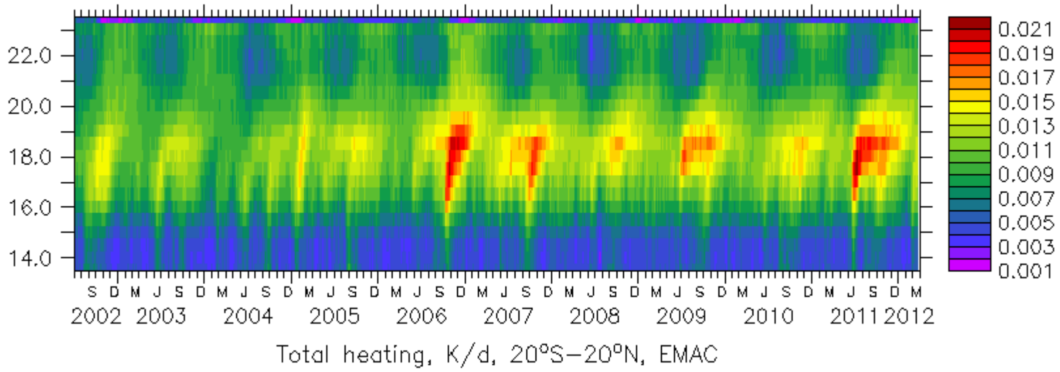

Figure 5: Simulated aerosol radiative heating in tropics (solar + infrared, T42, full dust).

4.4. Constraints from total aerosol optical depth in different spectral regions and for different aerosol subsets

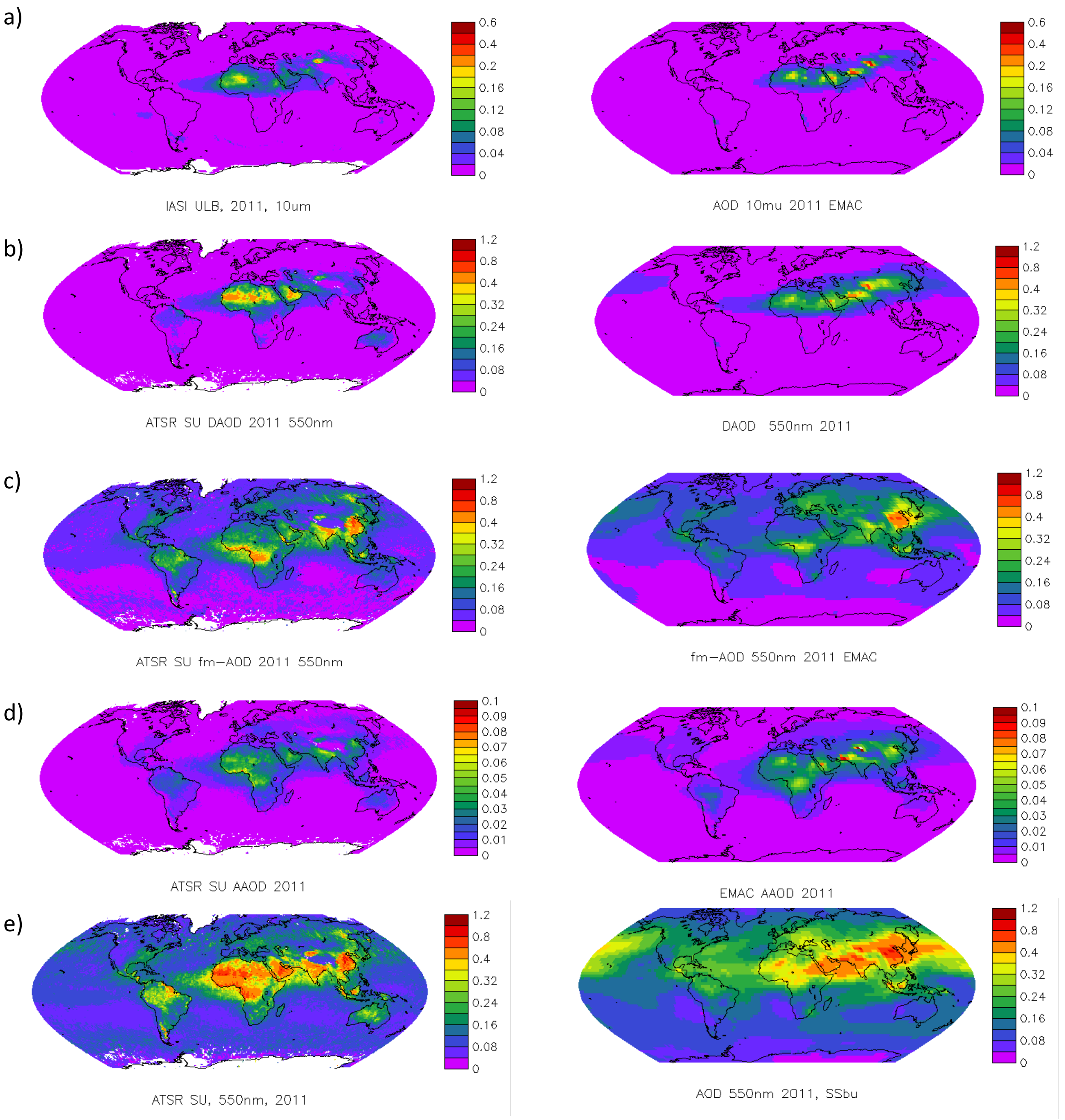

Figure 6: Observed (left) and simulated (right) (a): 10 µm AOD for IASI and EMAC; (b): and 0.55 µm dust aerosol optical depth (DAOD); (c): fine mode AOD; (d): absorbing AOD (AAOD) and (e): total AOD for ATSR (SU) and EMAC in T42L90 resolution.

The first comparisons are carried out for EMAC in T42L90, the standard resolution used in the previous sections. The AOD in terrestrial infrared is most sensitive to the coarse mode of tropospheric dust. Fig. 6 (a) shows that the model reproduces most of the IASI features but overestimates the AOD in the Himalaya region. This feature appears also in DAOD in the visible spectral region (b), pointing also to an overestimate of dust in the accumulation mode near the Taklamakan desert. The fine mode AOD fraction is overestimated over Europe (c). In the model this is sensitive to the way how the extinction of aerosol water is attributed to the soluble aerosol species, especially sea salt. Absorbing AOD, i.e. AOD times (1-ω) with ω single scattering albedo, agrees surprisingly well (d). In the total AOD (e) there appears to be too much sea salt in the model or still not optimum parameters for the sea salt composition which controls water uptake.

Figure 7 compares the annual average for 2011 of the 10 µm DAOD observed by IASI and simulated by EMAC in the low top version with high horizontal resolution (T106, about 1.1°). The satellite retrievals are taken from version 8 of the ULB dataset. The simulation utilizes the dust emission scheme of Klingmüller et al. (2018) which calculates the emissions online considering the meteorological conditions. To extract the DAOD from the total EMAC AOD at 10 µm, we apply a filter nullifying sea salt dominated AOD values. To identify the latter, we compare the AOD weighted with the volume of sea salt and dust.

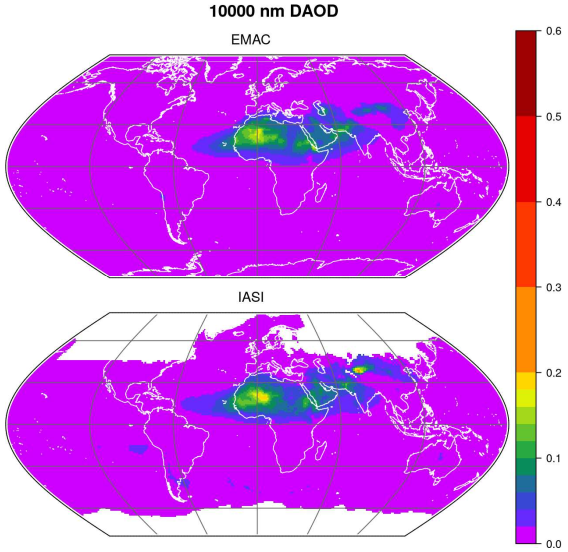

Figure 7: Annual mean for 2011 of the DAOD at 10 µm wavelength observed by IASI (bottom, IASI ULB dataset version 8) and simulated by EMAC (top) at T106 horizontal resolution (about 1.1°) using 31 vertical levels.

The observed and modelled global DAOD distributions shown in Fig. 7 agree remarkably well. The pixel values of each map are strongly correlated with a correlation coefficient of 0.91. The overall AOD level is consistent as well, so that a similar variance of the pixel values is obtained for the observed (0.00038) and the modelled (0.00041) DAOD distribution. Interestingly, the DAOD from the older version 7 of the ULB dataset yields a pixel by pixel correlation coefficient of only 0.89 and a pixel value variance of only 0.00029. We conclude that the agreement of EMAC and IASI has improved with the update from version 7 to version 8 of the IASI ULB dataset.

The main disagreement of the two maps in Fig. 7 is the less pronounced maximum over the Taklamakan Desert in Central Asia in the model result. This underestimation is related to the model surface friction velocity in mountainous regions like the surroundings of the Taklamakan Desert, which tends to be lower in simulations at higher resolution (e.g. T106) than at lower resolution (e.g. T42), possibly resulting in an underestimation of the dust emissions.

Figure 8 compares results from the T106L31 EMAC simulation for the annual average of the total AOD at visible and near-infrared wavelengths with AASTR retrievals using the ATSR (SU) algorithm version 4.3. Generally good agreement is obtained at 550 nm which is consistent with the good agreement between the 550 nm MODIS (Moderate-resolution Imaging Spectroradiometer) AOD and model results based on the same EMAC version (Klingmüller et al., 2018). As for the T42L90 simulation, the model yields higher sea salt related AOD levels over the oceans. In contrast, the model AOD over the Sahara is lower than the satellite retrieved values. This becomes even more evident at larger wavelengths (Fig. 8, right): the model AOD over the Sahara, in contrast to most other regions, has a stronger wavelength dependence than the observed AOD, corresponding to a larger Ångström exponent. This discrepancy might be resolved by adjusting the dust particle size distribution in the model under the constraint of not sacrificing the good agreement of model and observed AOD at 550 nm and at 10 µm. Over South America, the biomass burning regions of Africa, India and China the wavelength dependence of model and observed AOD is largely consistent.

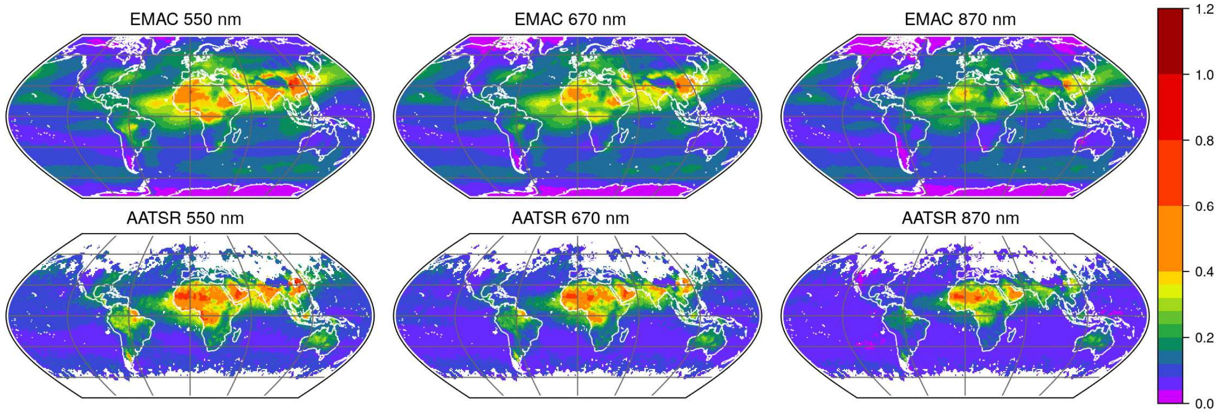

Figure 8*:* Annual mean for 2011 of the AOD at (from left to right) 550 nm, 670 nm and 870 nm wavelength observed by AATSR (bottom, SU-ATSR algorithm version 4.3) and simulated by EMAC (top) at T106 horizontal resolution (about 1.1°) using 31 vertical levels

5 Conclusions

Satellite data are not only important to constrain model parameters; they are very important for model development.

Sophisticated modelling of dust and organic aerosol as well as a detailed volcano dataset are necessary to reproduce extinction in the lowermost stratosphere observed by GOMOS at different wavelengths (Bingen et al., 2017). The scaling of EMAC dust AOD in the stratosphere by 0.33 was done to correct for an artifact of convective transport in the resolution T42 which is not apparent in the higher resolution T63. The additional (ongoing) simulations with higher resolution were stimulated by the satellite observations.

The total AOD in the visible spectral range is very sensitive to aerosol water and the composition of sea salt. In the modal model, the bulk fraction has to be increased compared to ions to reduce artifacts of too much water uptake by sea salt. The satellite data help to find the best choice of parameters.

Simulated dust total aerosol optical depth agrees with satellite data in the visible (ATSR SU) and the infrared (IASI ULB, version 8). The combined comparison at visible and infrared wavelengths provides strong constraints on the modelled particle size distribution. The direct comparison of observations and model reveals different structures in the extinction patterns at both spectral ranges. From this, we conclude that simply assuming a factor of 2 for conversion of AOD from 10 µm to 550 nm is too crude.

Dust and volcanic eruptions based on satellite datasets help the model to get closer to observationally based estimates for radiative forcing, showing the interest of a close interaction between modelling and observation research teams.

Acknowledgements: This study was funded by the Aerosol CCI project, phase II, of the ESA Climate Change Initiative, as a user option. The satellite data were provided by the Aerosol-CCI-database at ICARE, Lille, France; the model simulations were performed at DKRZ, Hamburg, Germany, where also the results are stored.

References

Astitha. M., J. Lelieveld, M. Abdel Kader, A. Pozzer, and A. de Meij: Parameterization of dust emissions in the global atmospheric chemistry-climate model EMAC: impact of nudging and soil properties, *Atm.Chem.Phys. 12*, 11057–11083, 2012.

Bertaux, J.-L.; Kyrölä, E.; Fussen, D.; Hauchecorne, A.; Dalaudier, F.; Sofieva, V.; Tamminen, J.; Vanhellemont, F.; Fanton d'Andon, O.; Barrot, G.; et al.: Global ozone monitoring by occultation of stars: An overview of GOMOS measurements on ENVISAT. *Atmos. Chem. Phys. 10*, 12091–12148, 2010.

Bevan, S., North, P., Los, S. & Grey, W.: A global dataset of atmospheric aerosol optical depth and surface reflectance from AATSR. *Remote Sensing of Environment 116*, 199-210, 2012.

Bingen, C., Robert, C. E., Stebel, K., Brühl, C., Schallock, J., Vanhellemont, F., Mateshvili, N., Höpfner, M., Trickl, T., Barnes, J. E., Jumelet, J., Vernier, J.-P., Popp, T., de Leeuw, G., and Pinnock, S.: Stratospheric aerosol data records for the climate change initiative: Development, validation and application to chemistry-climate modelling. *Remote Sensing of Environment, 203*, 296-321, 2017.

Bourassa, A. F., L. A. Rieger, N. D. Lloyd, and D. A. Degenstein: Odin-OSIRIS stratospheric aerosol data product and SAGE III intercomparison, *Atmos. Chem. Phys.*, *12*, 605–614, 2012.

Brühl, C., Lelieveld, J., Tost, H., Höpfner, M., Glatthor, N.: Stratospheric sulphur and its implications for radiative forcing simulated by the chemistry climate model EMAC. *J. Geophys. Res. Atmos. 120*, 2103–2118, 2015. doi.:10.1002/ 2014JD022430.

Gu, L. H., Baldocchi, D. D., Wofsy, S. C., Munger, J. W., Michalsky, J. J., Urbanski, S. P., et al.: Response of a deciduous forest to the mount Pinatubo eruption: Enhanced photosynthesis. *Science, 299*(5615), 2035-2038, 2003.

Jöckel, P., Tost, H., Pozzer, A., Brühl, C., Buchholz, J., Ganzeveld, L., Hoor, P., Kerkweg, A.,Lawrence, M.G., Sander, R., Steil, B., Stiller, G., Tanarhte, M., Taraborrelli, D., van Aardenne, J., Lelieveld, J.: The atmospheric chemistry general circulation model ECHAM5/MESSy1: consistent simulation of ozone from the surface to the mesosphere. *Atmos. Chem. Phys. 6*, 5067–5104, 2006.

Jöckel, P., Kerkweg, A., Pozzer, A., Sander, R., Tost, H., Riede, H., Baumgaertner, A., Gromov, S., Kern, B.: Development cycle 2 of the Modular Earth Submodel System (MESSy2). *Geosci. Model Dev. 3*, 717–752, 2010.

Jöckel, P., et al.: Earth System Chemistry integrated Modelling (ESCiMo) with the Modular Earth Submodel System (MESSy) version 2.51. *Geosci. Model Dev.*, *9*, 1153–1200, 2016.

Kinne, S., et al.: An AeroCom initial assessment – optical properties in aerosol component modules of global models, *Atmos. Chem. Phys.*, *6*, 1-22, 2006.

Klingmüller, K., Metzger, S., Abdelkader, M., Karydis, V. A., Stenchikov, G. L., Pozzer, A., and Lelieveld, J.: Revised mineral dust emissions in the atmospheric chemistry–climate model EMAC (MESSy 2.52 DU_Astitha1 KKDU2017 patch), Geosci. Model Dev., 11, 989-1008, https:/ /doi.org/10.5194/gmd-11-989-2018, 2018.

Kyrölä, E.; Tamminen, J.; Sofieva, V.; Bertaux, J.L.; Hauchecorne, A.; Dalaudier, F.; Fussen, D.; Vanhellemont, F.; Fanton d'Andon, O.; Barrot, G.; et al.: GOMOS O_3, NO_2, and NO_3 observations in 2002-2008. *Atmos. Chem. Phys. 10*, 7723-7738, 2010.

Montzka, S. A., P. Calvert, B. D. Hall, J. W. Elkins, T. J. Conway, P. P. Tans, and C. Sweeney: On the global distribution, seasonality, and budget of atmospheric carbonyl sulfide and some similarities with CO2, *J. Geophys. Res.*, *112*, D09302, 2007.

North, P.: Estimation of aerosol opacity and land surface bidirectional reflectance from ATSR-2 dual-angle imagery: Operational method and validation. *Journal of Geophysical Research 107*(D12), 2002.

Pringle, K. J., H. Tost, S. Message, B. Steil, D. Giannadaki, A. Nenes, C. Fountoukis, P. Stier, E. Vignati, and J. Lelieveld: Description and evaluation of GMXe: A new aerosol submodel for global simulations (v1), *Geosci. Model Dev.*, *3*, 391–412, 2010. doi:10.5194/gmd-3-391-2010.

Popp, T., de Leeuw, G., Bingen, C., Brühl, C., Capelle, V., Chedin, A., Clarisse, L., Dubovik, O., Grainger, R., Griesfeller, J., et al.: Development, production and evaluation of aerosol climate data records from European satellite observations (Aerosol_cci). *Remote Sens.,* 421, 2016.

Robert, C.E.; Bingen, C.; Vanhellemont, F.; Mateshvili, N.; Dekemper, E.; Tétard, C.; Fussen, D.; Zehner, C.; Thomason, L.W.; McElroy, C.T.; et al.: AerGOM, an improved algorithm for stratospheric aerosol extinction retrieval from GOMOS observations Part 2: Intercomparisons, *Atmos. Meas. Tech. 9*, 4701-4718, 2016. doi:10.5194/amt-9-4701-2016.

Santer, B. D., et al.: Volcanic contribution to decadal changes in tropospheric temperature, *Nat. Geosci.*, *7*, 185–189, 2014.

Solomon, S., J. S. Daniel, R. R. Neely III, J. P. Vernier, E. G. Dutton, and L. W. Thomason: The persistently variable "background" stratospheric aerosol layer and global climate change, *Science, 333*, 866–870, 2011.

Van Damme, M., Whitburn, S., Clarisse, L., Clerbaux, C., Hurtmans, D., and Coheur, P.-F.: Version 2 of the IASI NH_3 neural network retrieval algorithm: near-real-time and reanalysed datasets, *Atmos. Meas. Tech., 10*, 4905-4914, 2017. doi:10.5194/amt-10-4905-2017

Vanhellemont, F.; Mateshvili, N.; Blanot, L.; Robert, C.E.; Bingen, C.; Tétard, C.; Fussen, D.; Dekemper, E.; Sofieva, V.; Kyrölä, E.; et al.: AerGOM, an improved algorithm for stratospheric aerosol extinction retrieval from GOMOS observations Part 1: Algorithm development, *Atmos. Meas. Tech. 9*, 4687-4700, 2016. doi:10.5194/amt-9-4687-2016.

Whitburn, S., M. Van Damme, L. Clarisse, S. Bauduin, C. L. Heald, J. Hadji-Lazaro, D. Hurtmans, M. A. Zondlo, C. Clerbaux, and P.-F. Coheur: A flexible and robust neural network IASI-NH3 retrieval algorithm, *J. Geophys. Res. Atmos., 121*, 6581–6599, 2016. doi:10.1002/2016JD024828.